



### 저작자표시-비영리-동일조건변경허락 2.0 대한민국

이용자는 아래의 조건을 따르는 경우에 한하여 자유롭게

- 이 저작물을 복제, 배포, 전송, 전시, 공연 및 방송할 수 있습니다.
- 이차적 저작물을 작성할 수 있습니다.

다음과 같은 조건을 따라야 합니다:



저작자표시. 귀하는 원저작자를 표시하여야 합니다.



비영리. 귀하는 이 저작물을 영리 목적으로 이용할 수 없습니다.



동일조건변경허락. 귀하가 이 저작물을 개작, 변형 또는 가공했을 경우에는, 이 저작물과 동일한 이용허락조건하에서만 배포할 수 있습니다.

- 귀하는, 이 저작물의 재이용이나 배포의 경우, 이 저작물에 적용된 이용허락조건을 명확하게 나타내어야 합니다.
- 저작권자로부터 별도의 허가를 받으면 이러한 조건들은 적용되지 않습니다.

저작권법에 따른 이용자의 권리는 위의 내용에 의하여 영향을 받지 않습니다.

이것은 [이용허락규약\(Legal Code\)](#)을 이해하기 쉽게 요약한 것입니다.

[Disclaimer](#)

공학석사 학위논문

수직 벽 근처에서 상승하는 크기가 크고  
변형가능한 기포의 움직임에 대한 실험적 연구

Experimental investigation on a large deformable bubble  
motion rising in the vicinity of the vertical wall

2015년 2월

서울대학교 대학원

기계항공공학부

정 현 주

수직 벽 근처에서 상승하는 크기가 크고  
변형가능한 기포의 움직임에 대한 실험적 연구

Experimental investigation on a large deformable bubble  
motion rising in the vicinity of the vertical wall

지도 교수 박 형 민

이 논문을 공학석사 학위논문으로 제출함  
2014년 10월

서울대학교 대학원  
기계항공공학부  
정 현 주

정현주의 공학석사 학위논문을 인준함

2014년 12월

위 원 장 \_\_\_\_\_ (인)

부위원장 \_\_\_\_\_ (인)

위 원 \_\_\_\_\_ (인)

# Experimental investigation on a large deformable bubble motion rising in the vicinity of the vertical wall

Hyeonju Jeong

Department of Mechanical & Aerospace Engineering  
Seoul National University

## Abstract

In the present study, the freely rising bubble behaviour near the vertical wall has been measured and analyzed while varying the wall configurations such as the initial distance between the bubble center and the wall and the wall material. The bubble Reynolds and Weber numbers are about 1100 and 4.4, respectively, based on the equivalent bubble diameter and these are relatively high values compared to those in the previous studies. The current bubble which has wobbling shape originally rises with a zig-zag trajectory indicating the two-dimensional movements. The initial distance between the bubble and the wall, and the surface boundary condition of the wall (no-slip, hydrophobic and porous, etc.) are considered to investigate the wall effect on the bubble motion. Though the bubble rises in the vicinity of the wall, the maintenance of two-dimensionality of the bubble rising path is confirmed while it is varied widely as bouncing, sliding and departing. In rising bubble motion, especially, the surface boundary condition significantly affects the bubble behaviour. So, first we analyze the rebounding

motion of the bubble fitting with the sinusoidal function and apply the relation between the energy components with the bubble motion. The energy dissipation shows different trends according to the initial distance and wall boundary conditions. The hydrophobic condition causes larger amount of energy dissipation than no-slip condition when the bubble slides on the wall and as  $s/r_{eq}$  increases (non-colliding motion appears), the dissipation has rather smaller value compared to no-slip condition. However, for the porous wall, the energy dissipation value is smallest among all conditions. Also, to deeply investigate the energy dissipation, the coefficient of restitution is calculated showing a good correlation with the variation of the energy components.

Keywords: bubble-wall interaction, wall effect, path instability, wall boundary condition, no-slip, slip, porous, bouncing, sliding, high-speed imaging technique

Student number: 2013-20717

# Contents

|   |      |
|---|------|
| Abstract  | i    |
| Contents  | iii  |
| List of Figures                                     | v    |
| Nomenclature  | viii |
| Chapter   |      |
| 1 Introduction                                      | 1    |
| 2 Experimental setup and procedure                  | 6    |
| 2.1 Experimental setup . . . . .                    | 6    |
| 2.2 Image processing. . . . .                       | 7    |
| 3 Results and Discussion                            | 11   |
| 3.1 Rebounding bubble ( $s^* < 2.0$ ). . . . .      | 11   |
| 3.2 Sliding bubble ( $s^* < 2.0$ ) . . . . .        | 12   |
| 3.3 Non-colliding bubble ( $s^* > 2.0$ ) . . . . .  | 15   |
| 3.4 Mean and instantaneous rise velocities. . . . . | 15   |
| 3.5 Bubble orientation. . . . .                     | 17   |
| 3.6 Variation in the energy components . . . . .    | 18   |
| 3.7 Coefficient of restitution . . . . .            | 20   |
| 4 Summary and Conclusion                            | 37   |
| Bibliography  |      |

## List of Figures

FIGURE 1.1 Streamwise vorticity (a) rectilinear path; (b) zigzag path; (b') same, half a period later; (c) spiral path. (Mougin & Magnaudet 2002)

FIGURE 2.1 (a) Experimental setup for a single bubble rising near a vertical wall in a stagnant water tank. (b) Reference zigzag motion of a freely rising bubble at  $Re \sim 1100$ . (c) Modeling of a periodically bouncing bubble's trajectory with a sinusoidal function and definition of bubble geometry.

FIGURE 2.2 Scanning electron microscopy (SEM) images ( $\times 100$ ) (top) and measurement of a contact angle (CA) of a water droplet (bottom) on the considered wall types: (a) polyurethane sponge; (b) regular PTFE; (c) roughened PTFE.

FIGURE 3.1 Variation in the trajectories (in  $x - y$  plane) of a rising bubble with  $s^*$  near the vertical wall of (a) acrylic; (b) polyurethane sponge; (c) PTFE and (d) roughened PTFE. The time interval between adjacent bubbles is 10 ms (i.e., 100 fps), being reduced from the raw 500 fps videos. The insets in the first column of (c) and (d) show the closed-up view of sliding bubble shape.

FIGURE 3.2 Variation in the trajectories (in  $x - z$  plane) of a rising bubble with  $s^*$  near the acrylic wall at a)  $90 < x^* < 165$ ; (b)  $10 < x^* < 80$ . The time interval between adjacent bubbles is 10 ms (i.e., 100 fps), being reduced from the raw 500 fps videos.

FIGURE 3.3 (a) Measured trace (symbols) of the and corresponding curve fit (lines):  $\circ$  and —, acrylic at  $s^* = 0.26$ ;  $\blacklozenge$  and  $-\cdot-\cdot-$ , polyurethane sponge at 0.26;  $\triangle$  and  $---$ , PTFE at 1.53;  $\blacksquare$  and  $\cdot\cdot\cdot$ , roughened PTFE at 2.04. Variations of the (b) normalized amplitude ( $h^*$ ) and (c) wavelength ( $\lambda$ ) with  $s^*$  are plotted for acrylic ( $\circ$ ), PTFE ( $\triangle$ ), roughened PTFE ( $\blacksquare$ ) and sponge ( $\blacklozenge$ ) walls, respectively. In (b) and (c), dashed lines denote  $h^*$  and  $\lambda$  of a freely rising bubble (i.e., without the wall) at the same  $Re$  and  $We$ . Here, superscript ‘\*’ denotes the normalization by the equivalent bubble radius ( $r_{eq}$ ).

FIGURE 3.4 Conceptual schematic to describe the thinning liquid layer between the rising bubble and the wall. Here the driving force ( $F$ ) is originated from the circulation by the vortices in the bubble wake.

FIGURE 3.5 Typical movement of a bubble when it is closest to the wall during its oscillatory rising trajectory, which includes bouncing and sliding, depending on wall type at  $s^* =$  (a) 0.26; (b) 1.02, and (c) 2.04. (d) Definition of the inclination angle ( $\beta$ ). In (a–c), the solid lines over the bubbles illustrate the horizontal axis ( $d_h$ ) of the bubble.

FIGURE 3.6 Variation of inclination angle ( $\beta$ ) with bubble trajectory: (a) acrylic wall at  $s^* = 0.26$ ; (b) at 4.08; (c) polyurethane sponge wall at 0.26; (d) at 4.08; (e) PTFE wall at 1.02; (f) at 4.08; (g) roughened PTFE wall at 2.04; (h) at 4.08. Here,  $\circ$  and the solid line denote  $\beta$  and trajectory of bubble center,

respectively.

FIGURE 3.7 History of instantaneous velocity of rising bubble near the (a,c,e,g) acrylic and (b,d,f,h) polyurethane sponge walls, at  $s^* =$  (a,b) 0.26; (c,d) 1.53; (e,f) 2.55; (g,h) 4.08. Here,  $\circ$  and  $\bullet$  denote the vertical ( $u$ ) and wall-normal ( $v$ ) components of the velocity, respectively, and the solid lines show the corresponding trajectory of the bubble center. In (a)–(c), the dashed-line boxes highlight the bubble-wall collision.

FIGURE 3.8 History of instantaneous velocity of rising bubble near the (a,c,e,g) PTFE and (b,d,f,h) roughened PTFE walls, at  $s^* =$  (a,b) 0.26; (c,d) 1.53; (e,f) 2.55; (g,h) 4.08. Here,  $\circ$  and  $\bullet$  denote the vertical ( $u$ ) and wall-normal ( $v$ ) components of the velocity, respectively, and the solid lines show the corresponding trajectory of the bubble center. In (a)–(c), the dashed-line boxes highlight the bubble-wall collision.

FIGURE 3.9 Variation of the normalized mean rise velocity ( $u/U$ ) with  $s^*$ :  $\circ$ , acrylic;  $\blacklozenge$ , polyurethane sponge;  $\triangle$ , PTFE;  $\blacksquare$ , roughened PTFE walls.

FIGURE 3.10 Variations in energy components along  $x^*$  for acrylic wall at  $s^* = 0.26$ : i)  $\bullet$ ,  $E_{ku}/E_k$ ;  $\circ$ ,  $E_{kv}/E_k$ ; ii)  $\bullet$ ,  $E_{ku}/E_v$ ;  $\circ$ ,  $E_{kv}/E_v$ ;  $\triangle$ ,  $E_s/E_v$ ; iii)  $\bullet$ ,  $\chi$ ; iv)  $\blacksquare$ ,  $E_s$ ; v)  $\square$ ,  $E_v$ ; vi)  $\diamond$ ,  $E_D/E_{to}$ . In i), the solid lines denote the corresponding bubble trajectory.

FIGURE 3.11 Variations in energy components along  $x^*$  for polyurethane sponge wall at 0.26: i)  $\bullet$ ,  $E_{ku}/E_k$ ;  $\circ$ ,  $E_{kv}/E_k$ ; ii)  $\bullet$ ,  $E_{ku}/E_v$ ;  $\circ$ ,  $E_{kv}/E_v$ ;  $\triangle$ ,  $E_s/E_v$ ; iii)  $\bullet$ ,  $\chi$ ; iv)  $\blacksquare$ ,  $E_s$ ; v)  $\square$ ,  $E_v$ ; vi)  $\diamond$ ,  $E_D/E_{to}$ . In i), the solid lines denote the corresponding bubble trajectory.

FIGURE 3.12 Variations in energy components along  $x^*$  for PTFE wall at  $s^* = 1.02$ : i)  $\bullet$ ,  $E_{ku}/E_k$ ;  $\circ$ ,  $E_{kv}/E_k$ ; ii)  $\bullet$ ,  $E_{ku}/E_v$ ;  $\circ$ ,  $E_{kv}/E_v$ ;  $\triangle$ ,  $E_s/E_t$ ; iii)  $\bullet$ ,  $\chi$ ; iv)  $\blacksquare$ ,  $E_s$ ; v)  $\square$ ,  $E_t$ ; vi)  $\diamond$ ,  $E_D/E_{to}$ . In i), the solid lines denote the corresponding bubble trajectory.

FIGURE 3.13 Variations in energy components along  $x^*$  for roughened PTFE wall at 2.04: i)  $\bullet$ ,  $E_{ku}/E_k$ ;  $\circ$ ,  $E_{kv}/E_k$ ; ii)  $\bullet$ ,  $E_{ku}/E_t$ ;  $\circ$ ,  $E_{kv}/E_t$ ;  $\triangle$ ,  $E_s/E_t$ ; iii)  $\bullet$ ,  $\chi$ ; iv)  $\blacksquare$ ,  $E_s$ ; v)  $\square$ ,  $E_t$ ; vi)  $\diamond$ ,  $E_D/E_{to}$ . In i), the solid lines denote the corresponding bubble trajectory.

FIGURE 3.14 Variation of  $E_w/E_{to}$  with  $s^*$  in its (a) average and (b) maximum peak;  $\circ$ , acrylic;  $\blacklozenge$ , polyurethane sponge;  $\triangle$ , PTFE;  $\blacksquare$ , roughened PTFE walls.

FIGURE 3.15 Variation of the coefficient of restitution ( $\epsilon$ ) with the modified impact Stokes number ( $St^*$ ) for the rebounding and bouncing–sliding transition events;  $\circ$ , acrylic;  $\blacklozenge$ , polyurethane sponge;  $\triangle$ , PTFE;  $\blacksquare$ , roughened PTFE walls.

# Nomenclature

## Roman Symbols

|   |  |
|---|--|
| $d_{eq}$ ( $= (d_h^2 d_v)^{1/3}$ )            | equivalent bubble diameter                   |
| $h$   | bouncing amplitude                           |
| $St$ ( $= \rho_p d_{eq} u_{approach} / \mu$ ) | Stokes number of the bubble                  |
| $s$   | initial distance between the wall and bubble |
| $Re$ ( $= U_0 d_{eq} / \nu$ )                 | Reynolds number of the reference bubble      |
| $r_{eq}$ ( $= d_{eq} / 2$ )                   | equivalent bubble radius                     |
| $U_0$   | mean velocity of the reference bubble        |
| $\bar{u}$                                     | mean velocity of rising bubble               |
| $u$   | vertical velocity of the bubble              |
| $v$   | wall-normal velocity of the bubble           |
| $We$ ( $= \rho_l U_0^2 d_{eq} / \sigma$ )     | Weber number of the reference bubble         |

## Greek Symbols

|           |  |
|-----------|--|
| $\beta$   | inclination angle of the bubble        |
| $\lambda$ | bouncing amplitude                     |
| $\mu$     | dynamic viscosity                      |
| $\nu$     | kinematic viscosity                    |
| $\rho$    | density                                |
| $\sigma$  | surface tension at air-water interface |

## Subscripts

- ( )<sub>g</sub> property of air
- ( )<sub>l</sub> property of water

# Chapter 1

## Introduction

The hydrodynamic characteristics of the bubbly flows have been considered as important issues for decades due to the applicability for many applications such as the energy transfer systems and chemical reactors. In particular, the bubble of which diameter is larger than 10% of integral length scale of the flow substantially modulates the bubbly flow (Gore & Crowe 1989; Rensen *et al.* 2005; Balachandar & Eaton 2010; Hosokawa & Tomiyama 2013). Thus the bubbly flow has obtained many interests from the researchers, but there still have remained unsolved problems because of the difficulty of studying two phase flows. Among many issues, here we focus on the rise behaviour of a single bubble near the wall.

When the bubble size is small, it is regarded as the spherical shape and the flow around a sphere has been widely investigated. For small Reynolds number ( $Re \leq 130$ ), the flow is steady and has no oscillation behind the sphere (Sadatoshi 1956). However, at Reynolds number above about 270, the unsteady wake (double-thread wake) is generated and it transfers to the planar symmetric wake at  $300 \leq Re \leq 420$ . When the Reynolds number increases to about 3000, the flow around a sphere turns into the turbulent (Sakamoto *et al.* 1990).

On the other hand, the path instability of the unbounded single bubble has been studied by many researchers (Ellingsen & Risso 2001; Mougouin & Magnaudet 2002, 2006; Yang & Prosperetti 2007;

Zenit & Magnaudet 2008; Ern *et al.* 2012). For the small Reynolds and Weber numbers, the rising path of the bubble shows rectilinear trajectory whereas for the larger size of the bubble, the various trajectories (zig-zag, spiraling, etc) appear. This so-called path instability is strongly related to the wake instability of the bubble. As shown in figure 1.1, the axi-symmetric wake is induced behind the bubble which travels the rectilinear path. For zigzagging bubble, the planar symmetric wake is generated while changing its sign every half period and the vortex wrapping appears for the bubble which is in spiral path.

However, in actual applications, the events in which the rising bubble encounters the wall are frequently happened causing the complex interaction between the bubble and the wall. It has been revealed that the rising bubble near the wall has smaller velocity than unbounded bubble (Uno & Kinter 1956; Krishna *et al.* 1999). Also, de Vries (2001) has observed that the sliding or bouncing motion occur on a wall depending on the bubble size and the initial distance between the bubble and the wall. On the other hand, the serious analysis related to the wall effect on the hydrodynamics of the bubble-wall interaction is still unsolved. As previous studies, the researchers used the concept of the repulsive and attractive lift forces to explain the various rising motion near the wall at small Reynolds number ( $Re \leq 30$ ) (Takemura *et al.* 2002; Takemura & Magnaudet 2003). For slightly higher Reynolds number, the finite liquid velocity is induced between the bubble and the wall and the wall-normal pressure gradient by this velocity distribution attracts the bubble towards the wall (Takemura & Magnaudet 2003). As the bubble approaches to the wall, the sign of the lift force is reversed due to viscous effect in the liquid layer (lubrication theory) so that

the bubble bounces on the wall (Takemura & Magnaudet 2003; Sugiyama & Takemura 2010). However, for high Reynolds and Weber number bubble, this shape instability becomes more complex related to the shape instability (Magnaudet & Eames 2000). The bouncing motion of a spherical bubble in the vicinity of the wall is modeled by using the potential theory (Moctezuma *et al.* 2005). Zaruba *et al.* (2007) suggested the equation of the bubble rising motion at  $Re = 220 - 1000$  by considering the various force components. They imposed the different liquid velocity on the bubble and found that the rising bubble motion changes according to the liquid velocity.

Also for the horizontal wall, the bubble-wall collision dynamics has been investigated considering the different wall boundary conditions (Krasowska and Malysa 2007; Zawala *et al.* 2007). In particular, it is revealed that the slippery wall causes the rising bubble to attach to the wall after several collisions, due to the air pockets on the wall surface (Krasowska & Malysa (2007). The energy transfer from the kinetic energy to surface energy was small for hydrophobic surface indicating large energy loss (Zawala *et al.* 2007). Also, for the normal collision of the bubble, Zenit & Legendre (2009) investigated the coefficient of restitution which is the indirect measure of the energy loss due to the wall. The coefficient can be expressed with Stokes number and Capillary number and it can somehow explain the bubble motion in terms of variations in the energy components.

Although many studies have been conducted, there are some limitation of the bubble shape, size and small Reynolds number in previous studies. Also, the clear analysis which can cover all rising bubble motion is not yet found. So, in the present study, the path of

the single bubble near the vertical wall is experimentally investigated in a quiescent water tank. We used the bubble which has originally the path instability (two-dimensional zig-zag) without the wall and the large Reynolds number. We varied the initial distance between the bubble and the wall and the four different surface boundary conditions were imposed. We think that this analysis can help to understand the various bubble's rising motion in the vicinity of the wall and finally control the void fraction in bubbly flow.

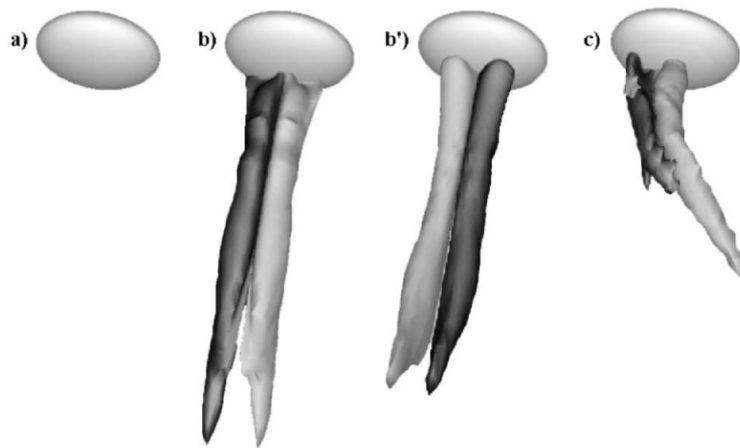


FIGURE 1.1 Streamwise vorticity (a) rectilinear path; (b) zigzag path; (b') same, half a period later; (c) spiral path. (Mougin & Magnaudet 2002)

# Chapter 2

## Experimental setup and procedures

### 2.1 Experimental setup

The experiments are conducted in the cube shaped acrylic water tank of which size is  $500 \times 500 \times 500 \text{ mm}^3$  as shown in figure 2.1 (a) and it's almost fully filled with the tap water. The air bubble comes from the air compressor through the regulator, solenoid valve and the stainless nozzle with 0.8 mm inner diameter and rises due to a buoyancy in quiescent water. The LED array with 532 nm of wavelength is placed at the back of the tank so that the bubble shadow is captured by the high speed camera (Troubleshooter, Fastec Imaging Co.). We set the bubble diameter as about 3.92 mm and corresponding Reynolds number is about 1100. In present condition, the shape of the bubble is oblate ellipsoid with approximated major axis ( $d_h$ ) and minor axis ( $d_v$ ). Also, the Weber and Eotvos numbers are respectively 4.4 and 2.1 and these non-dimensional numbers are relatively high values. In figure 2.1 (b), the freely rising (i.e., without the wall) single bubble path is shown with the front and side views and it confirms that the current bubble trajectory is zig-zag one which means a two-dimensionality. This kind of two-dimensional bubble trajectory can be fitted with the sinusoidal function as shown in figure 2.1(c) with the bouncing amplitude ( $h$ ) and wavelength ( $\lambda$ ).

As controllable parameters, the initial distance between the bubble and the wall, and different wall boundary condition are

considered. The normalized distance ( $s^*=s/r_{eq}$ ) varies from the 0.26 to 4.08 based on the bubble radius ( $r_{eq}$ ). For boundary condition, we conducted the experiments with acrylic (no-slip), PTFE (hydrophobic) and polyurethane sponge (porous) walls. For a hydrophobic wall, Teflon® is used as the commercial patented PTFE. Also, we obtained more enhanced hydrophobic condition by sanding the regular PTFE with an abrasive paper (grit No. 80). It is well known that the hydrophobicity increases by the addition of the roughness of the surface (Cassie & Baxter 1944). For each wall, the SEM images and the measured contact angles are presented at figure 2.2. As implied previously, the contact angle of roughened PTFE is modified from  $95^\circ$  to  $120^\circ$  by enhancing the hydrophobicity of the surface. Also, the root-mean-square size of the roughness is changed from about  $3.7 \mu\text{m}$  for regular PTFE to about  $42 \mu\text{m}$  for roughened PTFE, based on the cross-sectional SEM images.

## 2.2 Image processing

In the present study, the shadow images of a rising bubble are captured by a high-speed camera ( $640 \times 480$  pixels) at 500 fps. The spatial resolution of camera is set to be about  $280 \mu\text{m}$  per pixel so that the field of view has a size of  $177 \times 133 \text{ mm}^2$ , positioned at 20 mm above the nozzle exit.

The consecutive shadow images of the bubble are processed to analyze the shape and motion of the rising bubble by the method proposed by Broder & Sommerfeld (2007). First, the optimal threshold of the gray value is set to distinguish the bubble from the background. Then we apply the Sobel filter which evaluates the gray-value gradient on each pixel to detect the edge of the bubble.

Based on the detected contour of the bubble, we pick a number of points on the bubble on the bubble edge with a uniform spacing. By connecting all point on edge and a certain point inside the bubble, the bubble is divided into several segments. By calculating the center of gravity on each segment, the bubble center is determined.

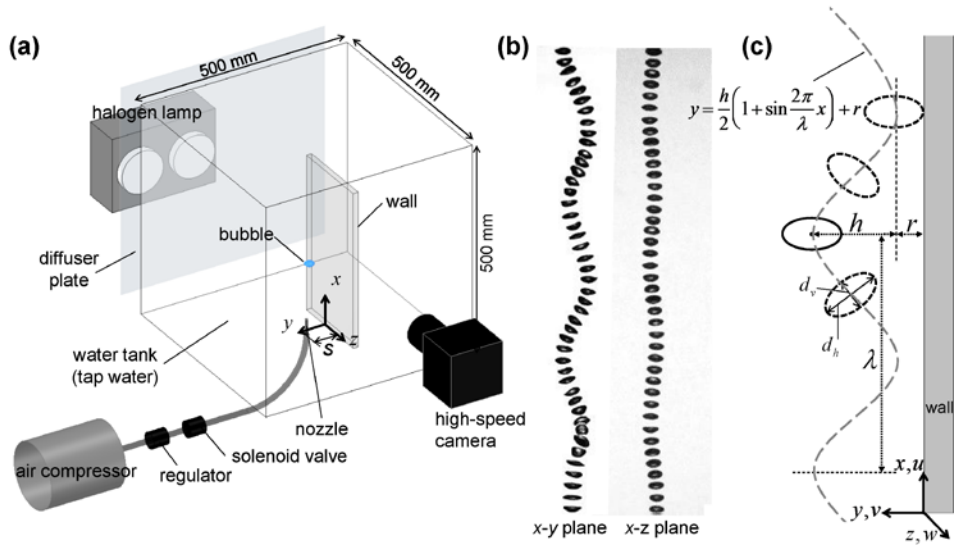


FIGURE 2.1 (a) Experimental setup for a single bubble rising near a vertical wall in a stagnant water tank. (b) Reference zigzag motion of a freely rising bubble at  $Re \sim 1100$ . (c) Modeling of a periodically bouncing bubble's trajectory with a sinusoidal function and definition of bubble geometry.

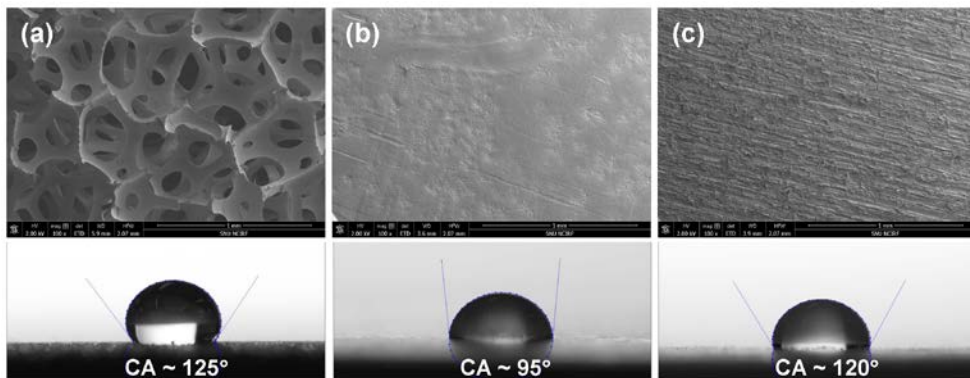


FIGURE 2.2 Scanning electron microscopy (SEM) images ( $\times 100$ ) (top) and measurement of a contact angle (CA) of a water droplet (bottom) on the considered wall types: (a) polyurethane sponge; (b) regular PTFE; (c) roughened PTFE.

# Results and Discussion

In this chapter, we discuss the various conditions of wall effect on the rising bubble in stagnant water and the representative results are shown in figure 3.1. To verify the two-dimensional bubble motion, we captured both front view and side view in figure 3.2. As shown in figure 3.2, the two-dimensional motion appears even after the bubble collides with the wall. So, we consider two-dimensional bubble rising motion and discuss the how the wall affects the rising bubble.

First, we look into the rebounding motion of the bubble in sec. 3.1 and the sliding motion in sec. 3.2 at small initial distance. As the initial distance increases, the bubble does not collide with the wall and non-colliding bubble is explained in sec. 3.3. Also, the mean and instantaneous rise velocities are calculated and analyzed in sec. 3.4 showing the good correlation with the trajectory. When collision occurs, the bubble rolls over the wall surface while showing the variation of inclination angle. So, the inclination angle is calculated in Sec 3.5. The energy interplay between the bubble and the wall is suggested in sec 3.6 and corresponding to this the coefficient of restitution is calculated in sec 3.7.

## 3.1 Rebounding bubble ( $s^* < 2.0$ )

For acrylic and polyurethane sponge wall, the rising bubble shows periodic or non-periodic rebounding motion near the wall at  $s^* < 2.0$ . We assumed that the bouncing motion occurs when the

distance between the bubble and the wall is smaller than the equivalent bubble radius. As shown in figure 3.3(a), the sinusoidal function is nicely fitted with the trajectories and the parameters of rebounding motion (amplitude, wavelength, etc.) were plotted in figure 3.3(b) and (c).

For acrylic wall, the periodic bouncing motion occurs at  $s/r_{eq} \leq 1.53$  and transfer to non-periodic as the distance increases. For periodic bouncing, the amplitude and wavelength are regular and the amplitude values are similar to that of the unbounded single rising bubble case. But the wavelength increases as the distance increases showing consistent trends and this behaviour remarkably appears at  $s^* = 2.04$ .

The rising bubble near the polyurethane sponge wall also regularly bounces off the wall at  $s^* \leq 1.02$ . The overall trends are almost similar to that of acrylic wall case but the amplitude and wavelength are noticeably smaller than acrylic wall. For polyurethane sponge, it has been considered to have slip velocity in tangential direction (Beavers *et al.* 1967; Hahn *et al.* 2002; Gangloff Jr. *et al.* 2014).

### 3.2 Sliding bubble ( $s^* < 2.0$ )

For PTFE wall which has a hydrophobicity, completely different behaviour appears. At  $s^* \leq 0.51$ , the bubble slides on the wall with slanted shape. In the previous study, it is observed that the spherical bubble also slides on the wall (ref) but the case is different from previous study that the bubble size is smaller than the current one. As  $s^*$  increases the bubble starts to collide with the wall showing a periodic bouncing motion as previous cases.

When we imposed the roughness on the PTFE, the hydrophobicity is enhanced (ref). Still, at small  $s^*$  ( $\leq 1.53$ ), the bubble slides on the wall but with more compressed shape towards the wall as shown in inset of figure 3.3(d). For enhanced hydrophobic wall, the sliding motion occurs in broader region than normal hydrophobic wall and interestingly, as  $s^*$  increases, the bubble initially bounces on the wall but the amplitude gradually becomes small and finally slides on the wall ( $s^* = 2.04$ ). This bouncing–sliding transition appears at  $1.02 \leq s^* \leq 2.04$ . At  $s^* = 2.55$ , also the bouncing amplitude of rising bubble becomes smaller and we guess this bubble will also finally slides.

As we mentioned, some previous studies suggested the mechanisms of sliding motion but current case is different due to the large diameter of the bubble. So, here we adopt the concept of three–phase contact to find the mechanism (criteria) of sliding bubbles. As the bubble approaches the wall, the liquid layer between the bubble and the wall becomes thinner as shown in figure 3.4. When the layer thickness is below than critical value, a three–phase (gas–liquid–solid) contact (TPC) is formed. The temporal rate of change in the thickness ( $h_l$ ) of the liquid layer between the solid wall and gas bubble (free surface) has been suggested by Sheludko (1967), as below:

$$\frac{d(1/h_l^2)}{dt} = \frac{16}{3\mu R_F^2} \Delta P \quad (3.1)$$

where  $\mu$  is the viscosity of the liquid,  $R_F$  is the radius of the liquid film, and  $\Delta P = (\approx 2 \sigma / r_{eq})$  is the difference between the pressures in the thin layer and in the bulk region. In equation (3.1),  $R_F = (r_{eq} / \pi \sigma) / F$ , where  $r_{eq}$  is the radius of the bubble,  $\sigma$  is the surface tension and  $F$  is the force causing the thinning of the liquid layer

(figure 3.4). For formation of TPC, the liquid layer between the bubble and the wall should reach a critical thickness of a rupture (Leja 1982; Nguyen *et al.* 2004). The critical thickness has been reported as  $O(\leq 1 \mu\text{m})$  (Schulze *et al.* 2001; Kraswska *et al.* 2009). Once the film ruptures, the TPC nucleus is formed and expanded to the TPC until the wetting perimeter of the bubble becomes long enough to make the bubble attach to the wall (Leja 1982; Nguyen *et al.* 2004).

As the driving force ( $F$ ), the wake-induced later force which is main cause of the path instability is considered. Since the velocity fields are not measured, we estimate driving force based on the circulation in the wake. So, the force is calculated by  $F \approx \rho_l u \Gamma r_{eq} = 2\pi \rho_l u r_{eq}^2 v_i$ , where  $u$  is the bubble's rise velocity. By integrating equation (3.1),

$$\frac{1}{h_l^2} \approx \frac{16}{3} \frac{\sigma^2}{\mu \rho_l u l^2 v_i r_{eq}^2} t \quad (3.2)$$

is obtained where  $t$  is the duration of bubble-wall collision. The collision time is decisive parameter of the film rupture and for acrylic wall, this value is about 10 msec which is short to form the TPC. As a result, the film thickness is estimated as  $h_l \approx 15-20 \mu\text{m}$ , which is one order of magnitude larger than the critical film thickness for rupture.

For roughened PTFE wall, the collision time is several times elongated ( $\geq 100$  msec) so that the film thickness is  $h_l \leq 3 \mu\text{m}$ , which is similar order to the critical thickness and finally the TPC formation occurs. As previously reported, there are air pockets on the hydrophobic surface due to the roughness and it encourages the formation of TPC. Therefore, we could reach the interesting result

that the way to make the bubble slides on the wall using hydrophobic surface.

### 3.3 Non-colliding bubble ( $s^* > 2.0$ )

As the distance between the wall and the bubble increases, the effect of the wall boundary condition on the bubble trajectory becomes smaller. Instead, the bubble shows a kind of irregular rise motions. For acrylic wall, at  $s^* \geq 2.55$ , the rising bubble does not touch the wall but oscillate irregularly. Basically, in current condition, the freely rising bubble without the wall has its own path instability which is zig-zag and the bubble rising motion shows similar behaviour when the bubble does not touch the wall. Also, for hydrophobic wall, as  $s^*$  increases, the rising bubble shows non-colliding motion and especially for enhanced hydrophobic wall, the oscillation amplitude gradually decreases.

Similar trends are shown for polyurethane sponge wall as  $s^*$  increases. However, compared to other case, at small  $s^*$  ( $\geq 1.02$ ), the rising bubble migrates away from the wall, which is considered as the result of the tangential slip condition of the wall.

### 3.4 Mean and instantaneous rise velocities

The variation of instantaneous bubble velocity (vertical ( $u$ ) and wall-normal ( $v$ ) components) is measured and shown in figure 3.7 and 3.8. In general, the wall-normal velocity is significantly varied according the oscillating bubble trajectory compared to vertical velocity although the absolute value is smaller than the vertical component.

For the rebounding bubble on the acrylic and sponge walls (at  $s^* = 0.26$ ) (figure 3.7(a) and (b)), the wall-normal velocity ( $v$ ) is accelerated as the bubble is attracted to the wall. Then  $v$  drops to the negative peak before the collision. From this moment on, during collision,  $v$  is instantly reduced and changes its sign to approach the positive (out of the wall) peak (highlighted with dashed-line boxes in figure 3.7a,b). as the bubble is shifted to the maximum distance from the wall after the collision,  $v$  is retained almost constant and the same process repeats as the bubble rebounds. After each collision significant reductions of  $u$  or  $v$  are not measured in the present condition. Since the bubble-wall contact time on the sponge wall is slightly longer than that on the acrylic wall, the rate of change in wall-normal velocity across the collision on the sponge wall is less sharp compared to the acrylic wall. Although, a slight deceleration of  $u$  is observed during the bubble-wall collision, its variation is not strong compared to that of  $v$ . As  $s^*$  increases, the unsteady scattering of  $u$  becomes more pronounced (figure 3.7e-h), which is consistent with the findings that the bubble trajectory is less regulated at  $s^* > 2.0$ .

On the other hand, for hydrophobic walls (figure 3.8), the different trends are observed while the bubble slides on the wall. The vertical ( $u$ ) velocity remains almost constant and the wall-normal ( $v$ ) velocity is close to zero value. For bouncing motion at higher  $s^*$ , the trends become similar to previous acrylic and sponge cases. At  $s^*=2.55$  for roughened hydrophobic wall, the bouncing-sliding transition occurs showing both sliding and rebounding characteristics, at a time.

To investigate the global effect of the wall boundary condition and initial distance, the mean rise velocities of the bubble are

plotted in figure 3.9. The velocities are normalized based on the reference bubble velocity (i.e. without the wall). As shown clearly, the velocities are decelerated due to the wall effect over the all regions which is consistent result with Uno & Kinter (1956) and Krishna *et al.* (1999). Here, two different regimes appear again. At  $s^* \leq 2.0$ , the rise velocities show scattered values according the wall boundary condition, indicating various bubble motion such as bouncing, sliding and departing. The rising bubbles which exist in this regime is highly affected by the wall configurations. For polyurethane sponge wall, the departing motion appears earlier and the rise velocity is highest among all conditions. The PTFE and roughened PTFE have smaller rise velocity than acrylic wall due to the sliding motion. However, at the second regime, these differences are reduced although there is small difference for PTFE. It indicates the wall effect decreases as the initial distance increases. On the other hand, the rise velocity is still slightly different from that of the unbounded bubble so it is regarded that the wall effect is not zero even at highest  $s^*$  we measured.

### 3.5 Bubble orientation

In present study, the bubble has an oblate ellipsoidal shape and its deformation greatly affects the rising motion especially when the bubble is closest to the wall. In figure 3.5, the closed-up views of rising motion of bouncing on each type of the wall are shown. The rising motions near each wall have different features when the collisions occur. Basically, the major axis of the rising bubble is perpendicular to moving direction but during the collision, the bubble rolls over the wall. To investigate the effect of the wall on

the bubble's orientation, we calculated the inclination angle ( $\beta$ ), defined as the angle between the horizontal axis and the vertical wall. For the bouncing motion, we choose a specific  $s^*$  at which the first bouncing motion appears for each wall. For the bouncing motion, the inclination angle increases as the bubble becomes close to the wall and decreases at the moment of collision. After the collision, the  $\beta$  recover as the bubble moves apart from the wall. This recovery process of polyurethane sponge wall is faster than acrylic wall and for hydrophobic surface this rapid change does not appear indicating the large wall effect. The inclination angle is about  $95^\circ \pm 12^\circ$  for acrylic,  $70^\circ \pm 10^\circ$  for the sponge,  $125^\circ \pm 15^\circ$  for the PTFE and  $144^\circ \pm 15^\circ$  for the roughened PTFE, respectively. So, for the porous wall, the smaller angular momentum is required compared to the no-slip wall due to the less rotating motion whereas the larger angular momentum is required for the hydrophobic wall. It is assumed that the energy transfer is somehow related to the rising bubble motion and it will be discussed next.

### 3.6 Variation in the energy components

During the various rising motions, the bubble interacts with the wall manifested as the energy transfer. As the bubble approaches the wall, the surrounding fluid is accelerated together (added-mass effect (Batchelor 1967; Clift *et al.* 1978) and the transports between the kinetic ( $E_k$ ), surface ( $E_s$ ) energies and to dissipation ( $E_D$ ) especially for the collision. We defined the above mentioned energies and the kinetic energy is as follows:

$$E_k = \frac{\pi}{12} (\rho_g + c_m \rho_l) d_{eq}^3 (u^2 + v^2) = E_{ku} + E_{kv} \quad (3.3)$$

where  $E_{ku}$  and  $E_{kv}$  denote the contribution of vertical and wall-normal velocities to  $E_k$ . For the added-mass coefficient ( $c_m$ ), we used a relation with the aspect ratio, as follows (Milne-Thomson 1968):

$$c_m = \frac{\alpha}{2-\alpha}, \quad \alpha = \frac{2\chi^2}{\chi^2-1} \left( 1 - \frac{1}{\sqrt{\chi^2-1}} \cos^{-1}(1/\chi) \right) \quad (3.4)$$

The aspect ratio ( $\chi = d_h/d_v$ ) is defined with the ratio of the length of horizontal (major) to vertical (minor) axis of the oblate ellipsoidal shape. On the other hand, in present study, the large surface energy is expected to contribute the energy transport due to the large deformation of the bubble shape. The surface energy is defined with  $E_s = \sigma A$  and  $\sigma$  is the surface tension at air-water interface. The surface area ( $A$ ) is expressed as a function of  $d_h$  and  $\chi$ , as below:

$$A = \frac{\pi d_h^2}{2} \left( 1 + \frac{1-e^2}{e} \tanh^{-1} e \right), \quad e^2 = 1 - 1/\chi^2 \quad (3.5)$$

We define  $E_t$  as a sum of kinetic and surface energies as  $E_t = E_{ku} + E_{kv} + E_s$ , then the energy would be balanced as  $E = E_t + E_D$  where  $E_D$  is the energy dissipation due to the viscosity and the wall effect. However, in the present study, because the liquid velocity data is not measured, we roughly estimated energy dissipation as the deficit of the  $E_t$  ( $E_D = E_{t0} - E_t$ ) where  $E_{t0}$  is the value of  $E_t$  when the bubble is displaced most far from the wall.

First, for the bouncing motion, due to the significant shape deformation, the aspect ratio greatly fluctuates while showing some correlation with the trajectory during its rise. As shown in second row of figure 3.8, the surface energy dominates the energy compared to the other energies. During the collision, the surface

energy increases as the bubble approaches the wall whereas the kinetic energy in vertical direction rather decreases and when the bubble migrates away from the wall, the opposite trends appear. The wall-normal kinetic energy and  $E_t$  rapidly increases before the collision and drops down to zero at collision moment and recovers some value after the collision indicating energy loss appears. Corresponding to this, the energy dissipation has a sharp peak at the collision moment as shown in figure 3.8 and 3.9.

Overall trends are similar for all bouncing events, however, for enhanced hydrophobic wall, the difference is observed. When the TPC formation occurs (as mentioned earlier), the  $E_t$  value is smaller than other cases and also the energy dissipation has large broad peak when the bubble attach to the wall. This energy dissipation has a key role to analyze the wall effect.

So, the normalized energy dissipation is plotted for all events in figure 3.12. As shown in figure, the energy dissipation becomes smaller as the distance increases indicating the wall effect decreases. Compared to no-slip surface, the rising bubble near the porous wall has smaller dissipation energy and it is consistent result with the highest rise velocity of sponge wall. For hydrophobic wall, the two regions appear based on the  $s^* = 2.55 - 3.06$ . The first region when the bubble slides on the wall, the large energy dissipation occurs and it is related to the TPC formation as previously mentioned. However, in second region, the energy dissipation value rather decreases and it is induced by the slip velocity on the surface due to the hydrophobicity.

### 3.7 Coefficient of restitution

We previously discussed the interplay between the energy storage and energy dissipation. The similar analysis is also performed for the normal bouncing motion of solid (Joseph *et al.* 2001; Gondret *et al.* 2002) and liquid (Legendre *et al.* 2005) particles onto a horizontal wall. The concept of the coefficient ( $\varepsilon$ ) of restitution is applied as an indirect measure of energy dissipation. The restitution coefficient is defined as  $\varepsilon = |v_{departure}/v_{approach}|$  and for solid particle, it is well correlated with the Stokes number ( $St = \rho_p d_{eq} v_{approach} / (9\mu)$ ) based on particle density,  $\rho_p$  (Joseph *et al.* 2001; Gondret *et al.* 2002). On the other hand, for liquid droplet, the modified Stokes number is suggested by Legendre *et al.* (2005) such as  $St = (\rho_p + c_m \rho) d_{eq} v_{approach} / (9\mu)$ .

Even though the concept of restitution coefficient is for normal bouncing, we think that it will be interesting to study the bubble-wall collision event in terms of  $\varepsilon$  and the result is shown in figure 3.13. As shown, even for the present lateral bubble-wall bouncings,  $\varepsilon$  is well presented with the modified Stokes number. The best fit equation is expressed as  $\varepsilon = \exp(5St^*)/30$ . Compared to the acrylic wall, the restitution coefficient for the sponge wall is larger indicating that the dominance of inertia over the viscous effect is more pronounced. However, for hydrophobic wall, the opposite trends appear indicating the larger energy loss and these results show consistency with the previous velocity data and energy analysis.

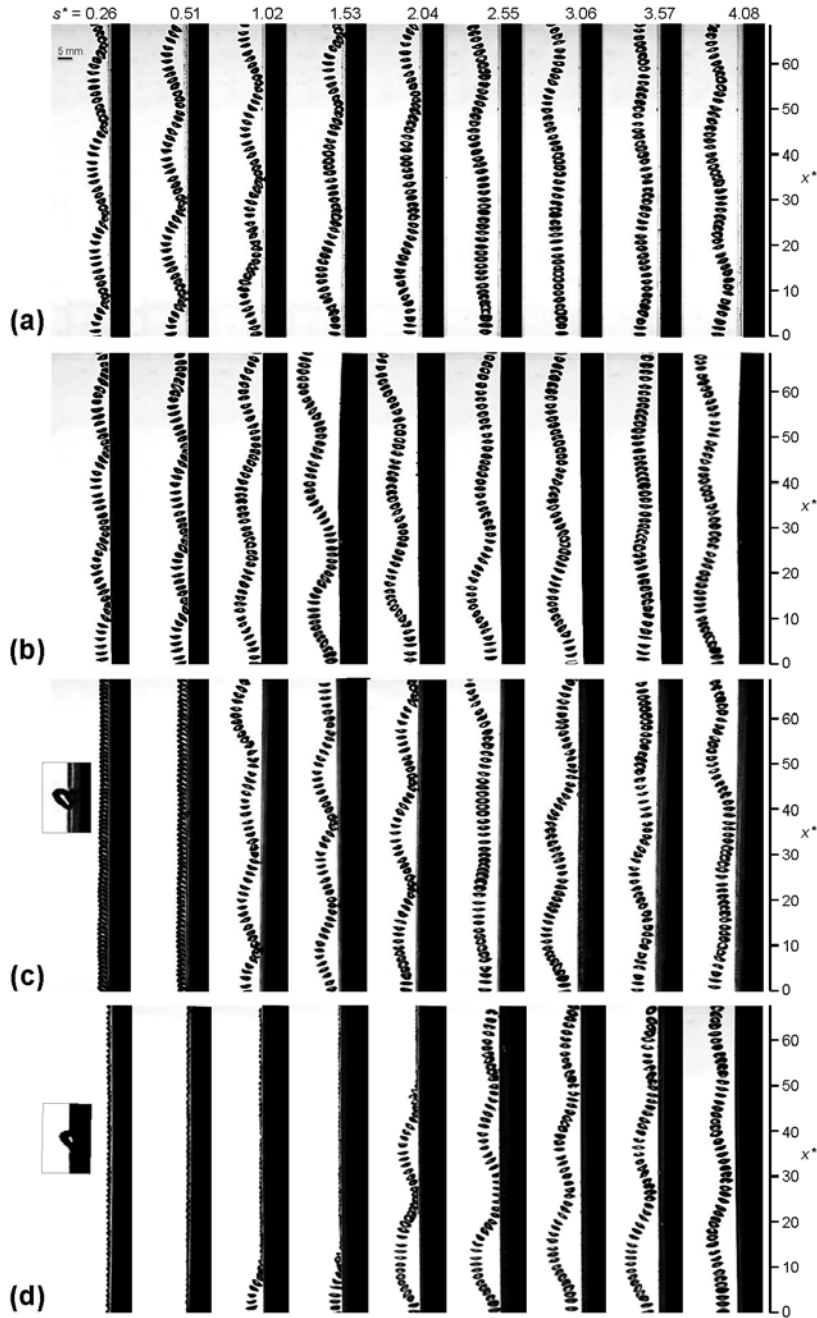


FIGURE 3.1 Variation in the trajectories (in  $x - y$  plane) of a rising bubble with  $s^*$  near the vertical wall of (a) acrylic; (b) polyurethane sponge; (c) PTFE and (d) roughened PTFE. The time interval between adjacent bubbles is 10 ms (i.e., 100 fps), being reduced from the raw 500 fps videos. The insets in the first column of (c) and (d) show the closed-view of sliding bubble shape.

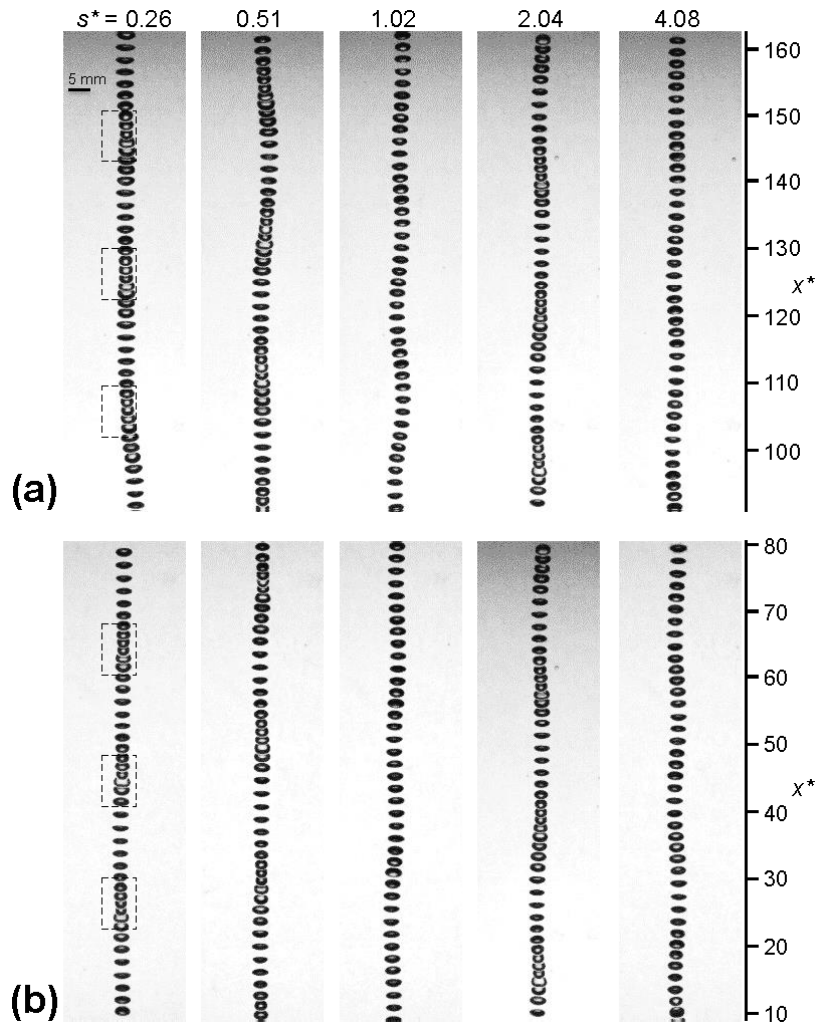


FIGURE 3.2 Variation in the trajectories (in  $x - z$  plane) of a rising bubble with  $s^*$  near the acrylic wall at a)  $90 < x^* < 165$ ; (b)  $10 < x^* < 80$ . The time interval between adjacent bubbles is 10 ms (i.e., 100 fps), being reduced from the raw 500 fps videos.

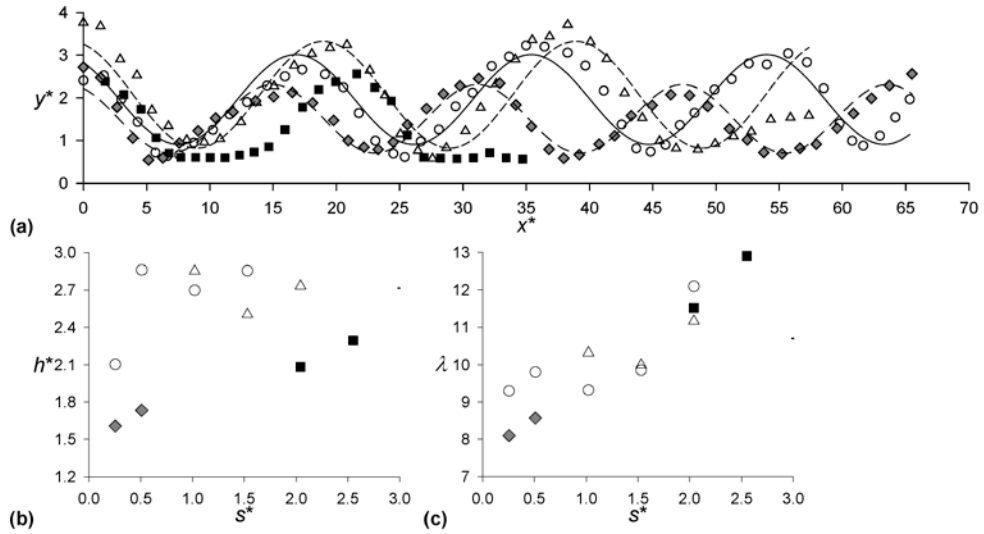


FIGURE 3.3 (a) Measured trace (symbols) of the and corresponding curve fit (lines):  $\circ$  and —, acrylic at  $s^* = 0.26$ ;  $\blacklozenge$  and - · - · -, polyurethane sponge at 0.26;  $\triangle$  and ---, PTFE at 1.53;  $\blacksquare$  and · · · · , roughened PTFE at 2.04. Variations of the (b) normalized amplitude ( $h^*$ ) and (c) wavelength ( $\lambda$ ) with  $s^*$  are plotted for acrylic ( $\circ$ ), PTFE ( $\triangle$ ), roughened PTFE ( $\blacksquare$ ) and sponge ( $\blacklozenge$ ) walls, respectively. In (b) and (c), dashed lines denote  $h^*$  and  $\lambda$  of a freely rising bubble (i.e., without the wall) at the same  $Re$  and  $We$ . Here, superscript ‘\*’ denotes the normalization by the equivalent bubble radius ( $r_{eq}$ ).

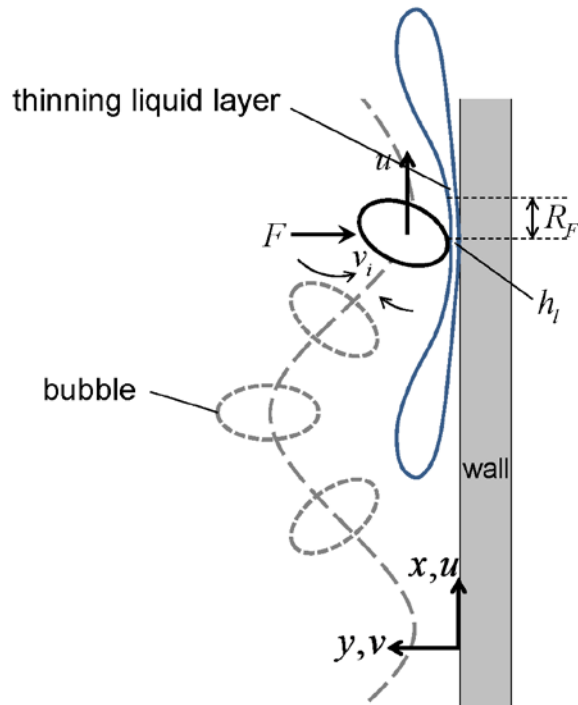


FIGURE 3.4 Conceptual schematic to describe the thinning liquid layer between the rising bubble and the wall. Here the driving force ( $F$ ) is originated from the circulation by the vortices in the bubble wake.

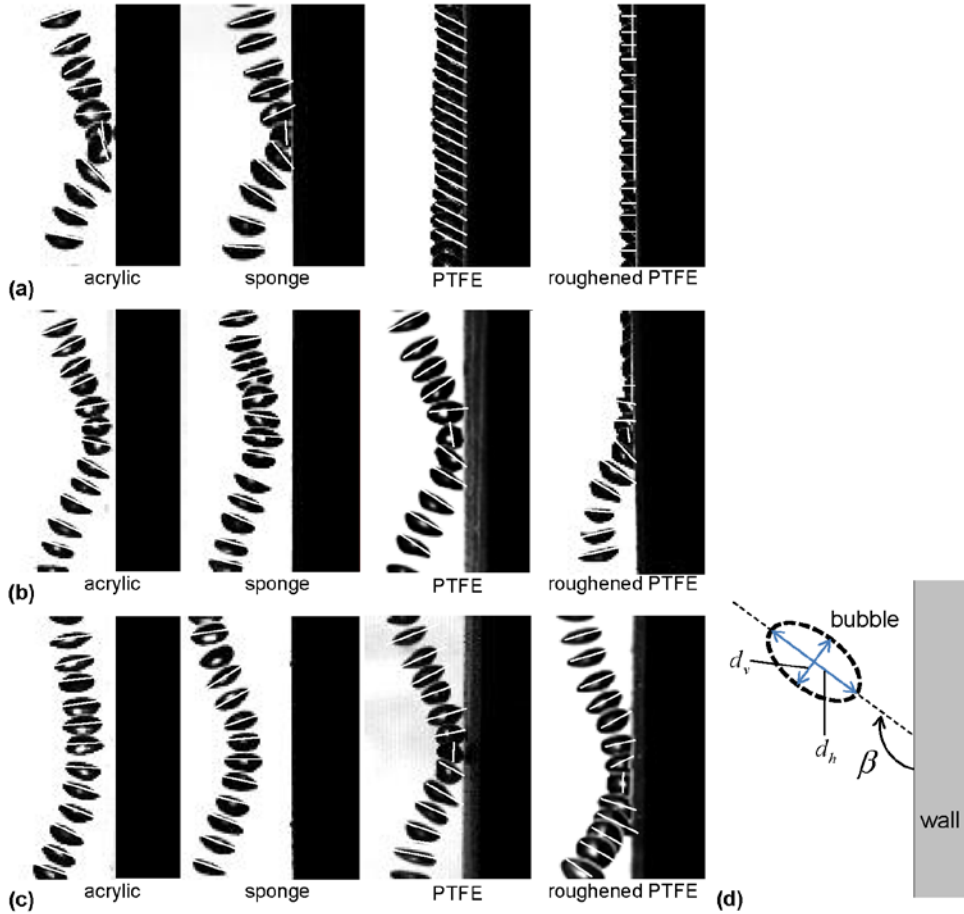


FIGURE 3.5 Typical movement of a bubble when it is closest to the wall during its oscillatory rising trajectory, which includes bouncing and sliding, depending on wall type at  $s^* =$  (a) 0.26; (b) 1.02, and (c) 2.04. (d) Definition of the inclination angle ( $\beta$ ). In (a–c), the solid lines over the bubbles illustrate the horizontal axis ( $d_h$ ) of the bubble.

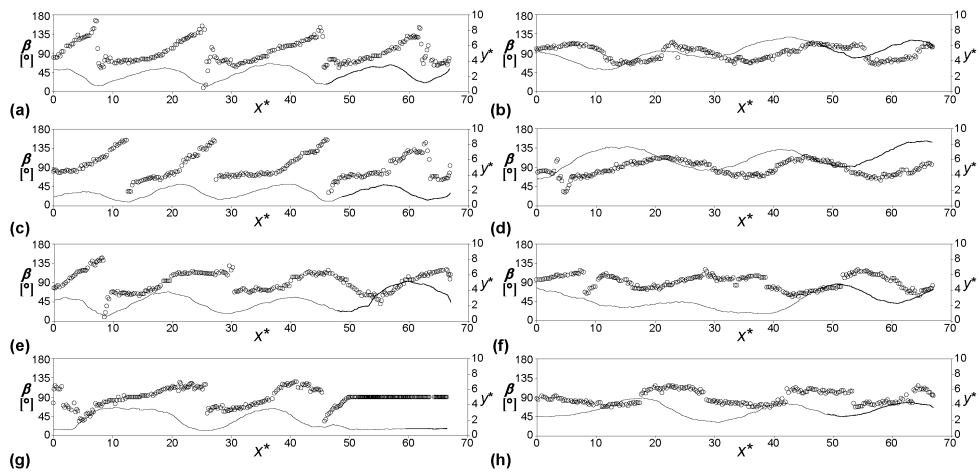


FIGURE 3.6 Variation of inclination angle ( $\beta$ ) with bubble trajectory: (a) acrylic wall at  $s^* = 0.26$ ; (b) at 4.08; (c) polyurethane sponge wall at 0.26; (d) at 4.08; (e) PTFE wall at 1.02; (f) at 4.08; (g) roughened PTFE wall at 2.04; (h) at 4.08. Here,  $\circ$  and the solid line denote  $\beta$  and trajectory of bubble center, respectively.

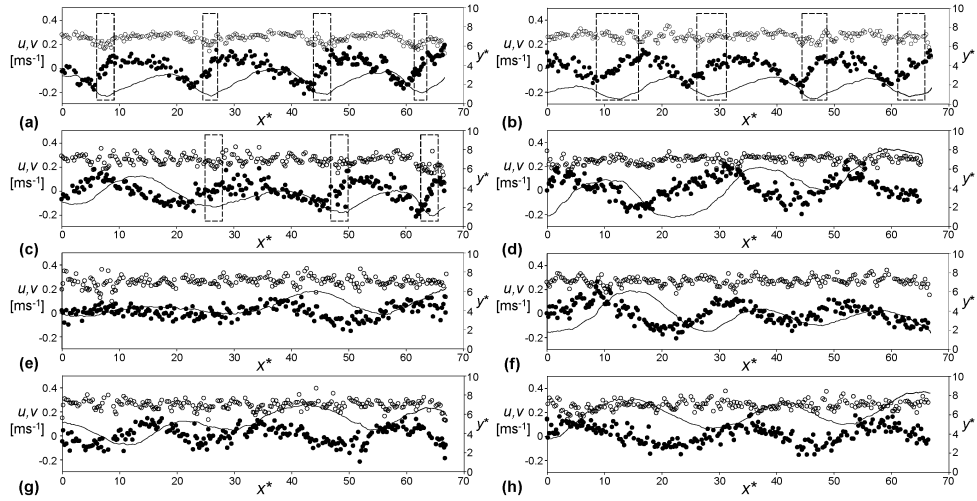


FIGURE 3.7 History of instantaneous velocity of rising bubble near the (a,c,e,g) acrylic and (b,d,f,h) polyurethane sponge walls, at  $s^* =$  (a,b) 0.26; (c,d) 1.53; (e,f) 2.55; (g,h) 4.08. Here,  $\circ$  and  $\bullet$  denote the vertical ( $u$ ) and wall-normal ( $v$ ) components of the velocity, respectively, and the solid lines show the corresponding trajectory of the bubble center. In (a)–(c), the dashed-line boxes highlight the bubble-wall collision.

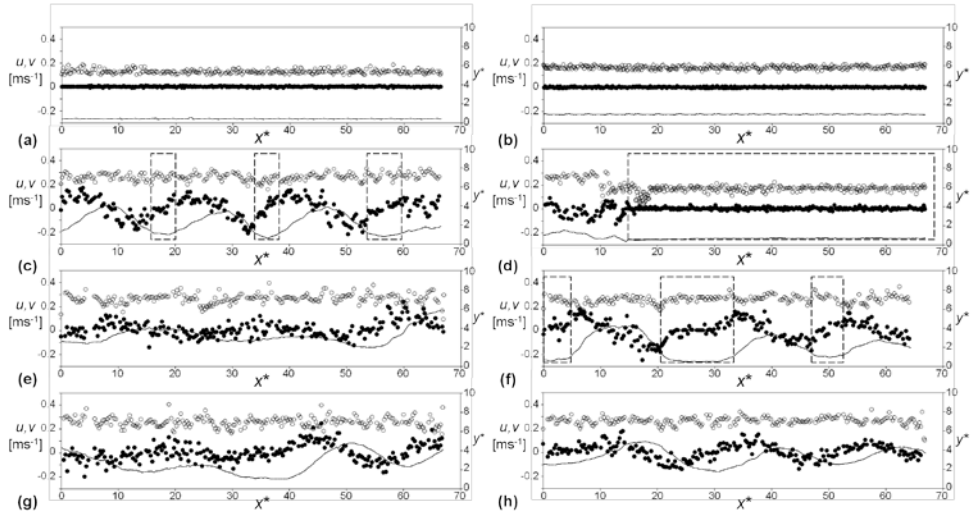


FIGURE 3.8 History of instantaneous velocity of rising bubble near the (a,c,e,g) PTFE and (b,d,f,h) roughened PTFE walls, at  $s^* =$  (a,b) 0.26; (c,d) 1.53; (e,f) 2.55; (g,h) 4.08. Here,  $\circ$  and  $\bullet$  denote the vertical ( $u$ ) and wall-normal ( $v$ ) components of the velocity, respectively, and the solid lines show the corresponding trajectory of the bubble center. In (a)–(c), the dashed-line boxes highlight the bubble-wall collision.

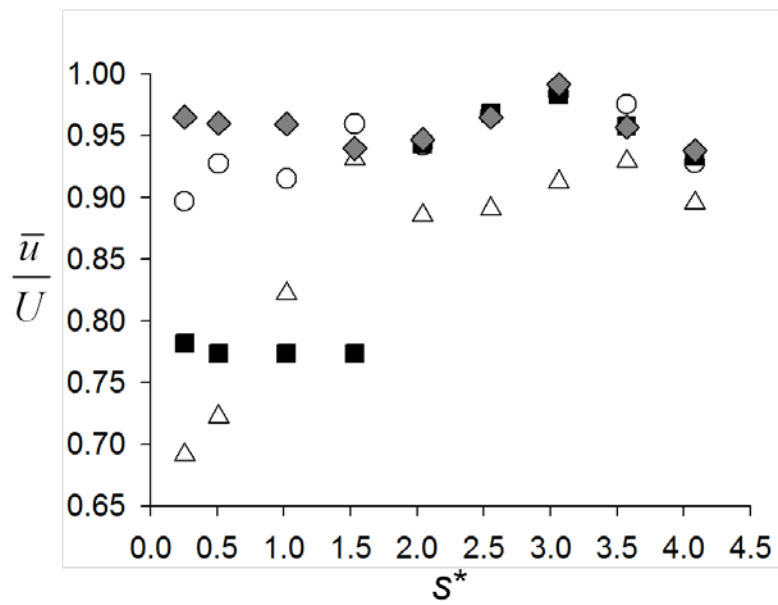


FIGURE 3.9 Variation of the normalized mean rise velocity ( $u/U$ ) with  $s^*$ :  $\circ$ , acrylic;  $\blacklozenge$ , polyurethane sponge;  $\triangle$ , PTFE;  $\blacksquare$ , roughened PTFE walls.

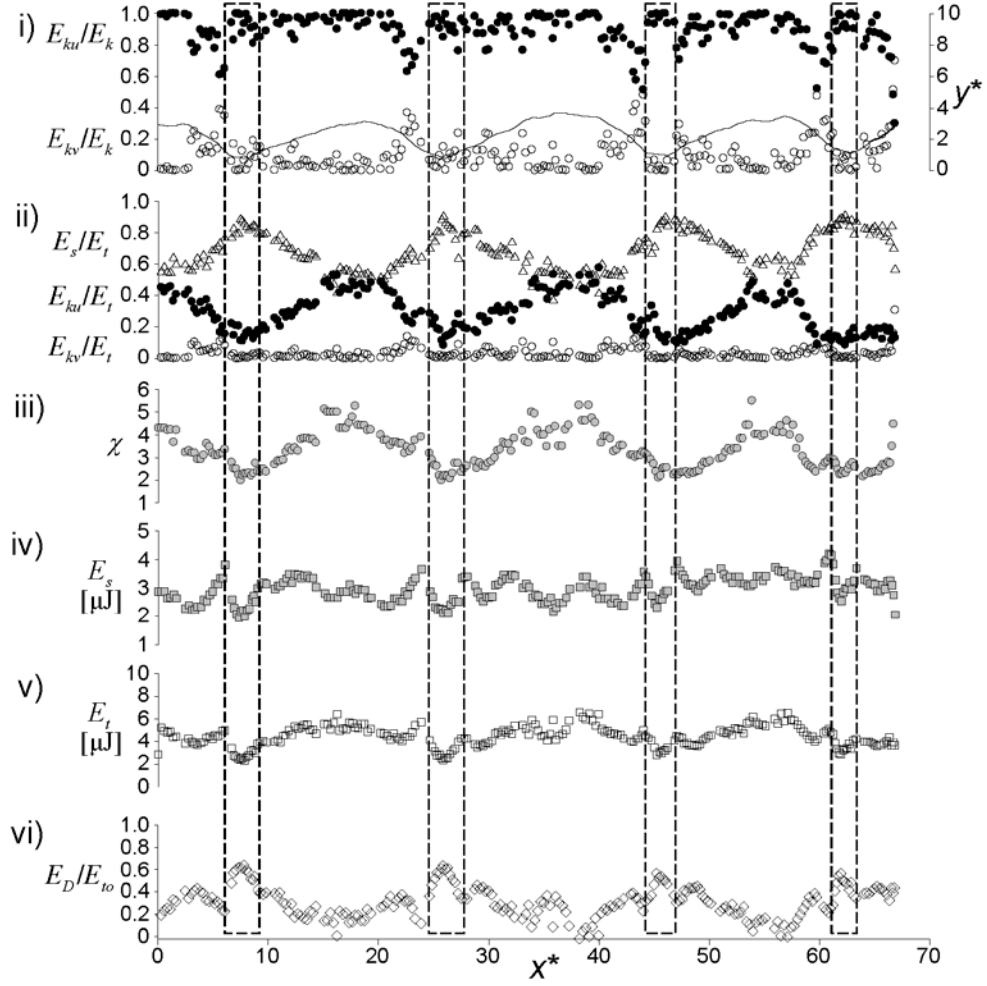


FIGURE 3.10 Variations in energy components along  $x^*$  for acrylic wall at  $s^* = 0.26$ : i)  $\bullet$ ,  $E_{ku}/E_k$ ;  $\circ$ ,  $E_{kv}/E_k$ ; ii)  $\bullet$ ,  $E_{ku}/E_t$ ;  $\circ$ ,  $E_{kv}/E_t$ ;  $\triangle$ ,  $E_s/E_t$ ; iii)  $\bullet$ ,  $\chi$ ; iv)  $\blacksquare$ ,  $E_s$ ; v)  $\square$ ,  $E_t$ ; vi)  $\diamond$ ,  $E_D/E_{to}$ . In i), the solid lines denote the corresponding bubble trajectory.

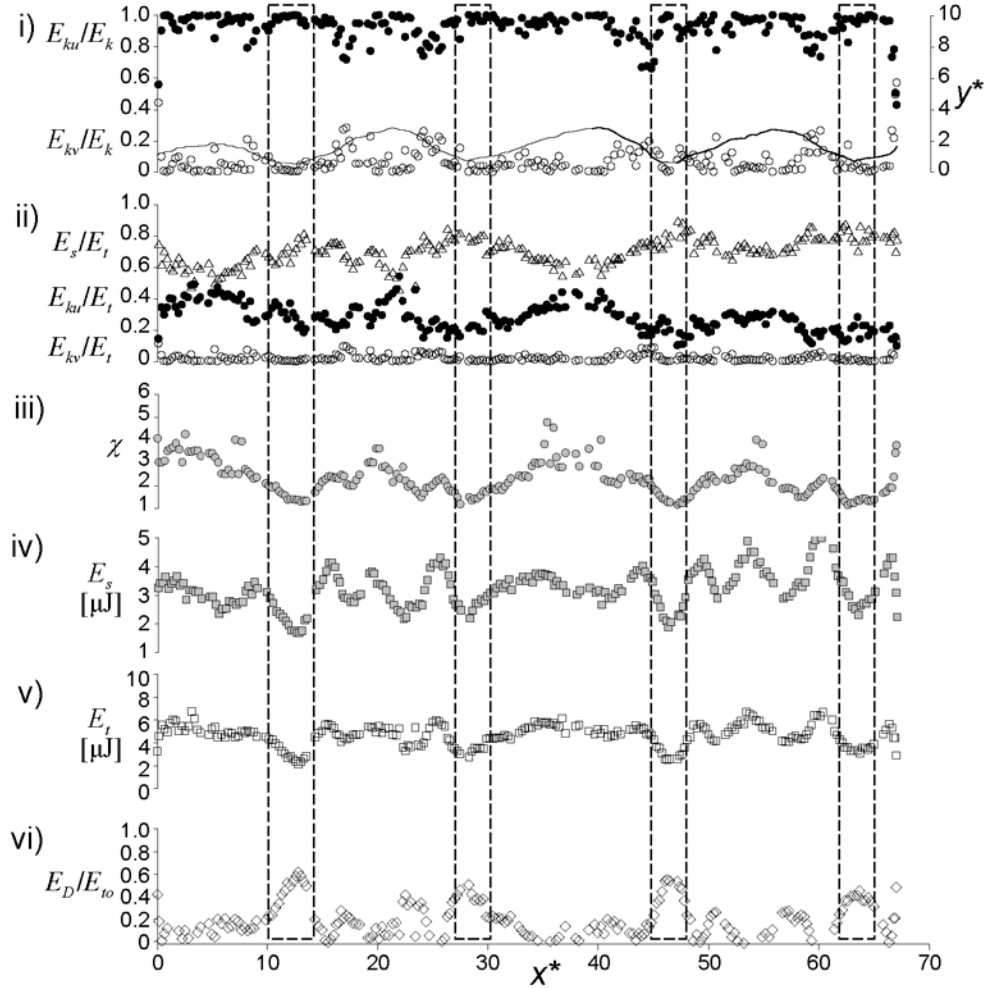


FIGURE 3.11 Variations in energy components along  $x^*$  for polyurethane sponge wall at 0.26: i)  $\bullet$ ,  $E_{ku}/E_k$ ;  $\circ$ ,  $E_{kv}/E_k$ ; ii)  $\bullet$ ,  $E_{ku}/E_t$ ;  $\circ$ ,  $E_{kv}/E_t$ ;  $\triangle$ ,  $E_s/E_t$ ; iii)  $\bullet$ ,  $\chi$ ; iv)  $\blacksquare$ ,  $E_s$ ; v)  $\square$ ,  $E_t$ ; vi)  $\diamond$ ,  $E_D/E_{to}$ . In i), the solid lines denote the corresponding bubble trajectory.

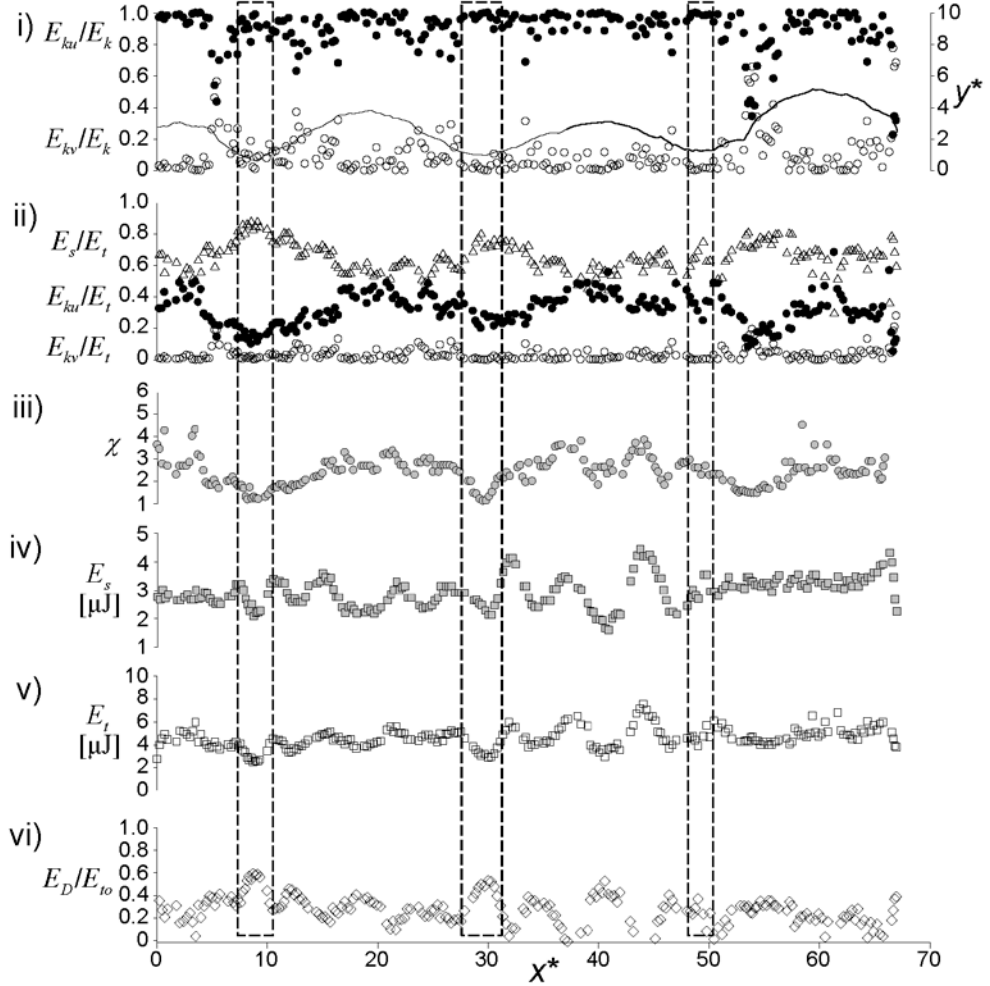


FIGURE 3.12 Variations in energy components along  $x^*$  for PTFE wall at  $s^* = 1.02$ : i)  $\bullet$ ,  $E_{ku}/E_k$ ;  $\circ$ ,  $E_{kv}/E_k$ ; ii)  $\bullet$ ,  $E_{ku}/E_t$ ;  $\circ$ ,  $E_{kv}/E_t$ ;  $\triangle$ ,  $E_s/E_t$ ; iii)  $\bullet$ ,  $\chi$ ; iv)  $\blacksquare$ ,  $E_s$ ; v)  $\square$ ,  $E_t$ ; vi)  $\diamond$ ,  $E_D/E_{to}$ . In i), the solid lines denote the corresponding bubble trajectory.

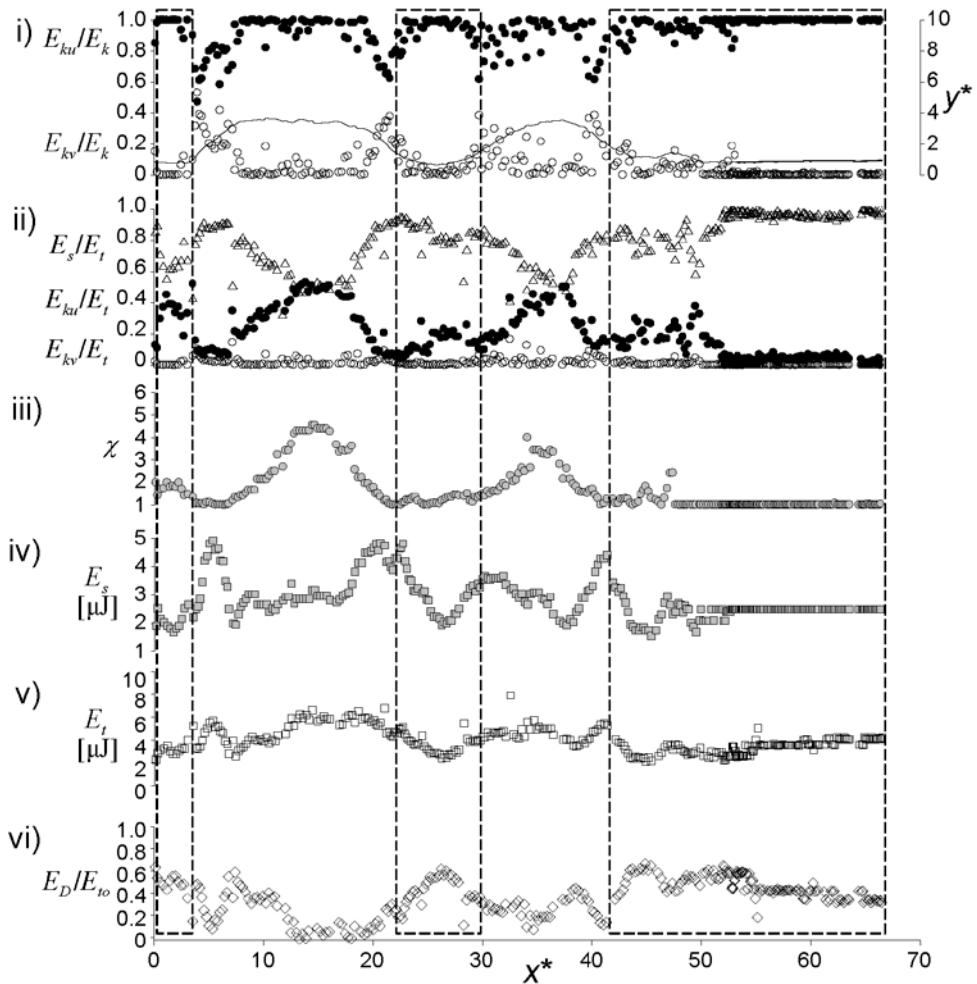


FIGURE 3.13 Variations in energy components along  $x^*$  for roughened PTFE wall at 2.04: i)  $\bullet$ ,  $E_{ku}/E_k$ ;  $\circ$ ,  $E_{kv}/E_k$ ; ii)  $\bullet$ ,  $E_{ku}/E_t$ ;  $\circ$ ,  $E_{kv}/E_t$ ;  $\triangle$ ,  $E_s/E_t$ ; iii)  $\bullet$ ,  $\chi$ ; iv)  $\blacksquare$ ,  $E_s$ ; v)  $\square$ ,  $E_t$ ; vi)  $\diamond$ ,  $E_D/E_{to}$ . In i), the solid lines denote the corresponding bubble trajectory.

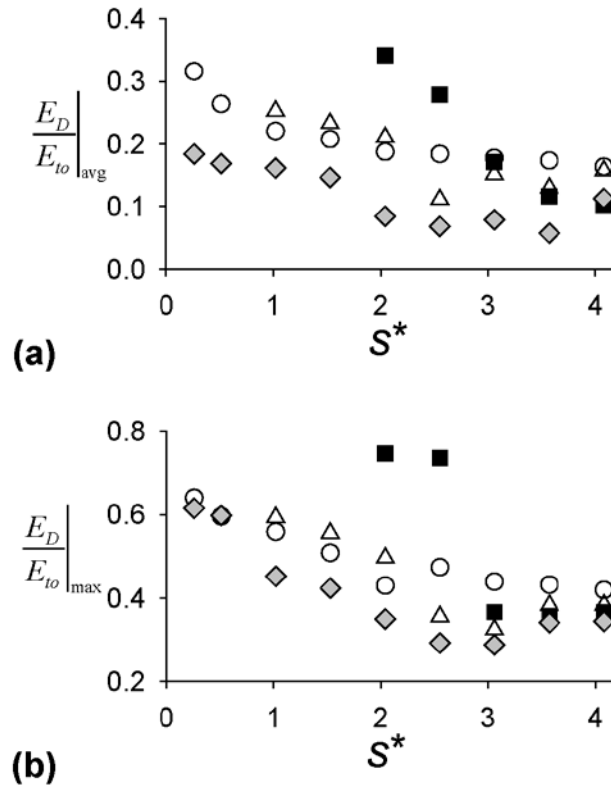


FIGURE 3.14 Variation of  $E_w/E_{to}$  with  $s^*$  in its (a) average and (b) maximum peak;  $\circ$ , acrylic;  $\blacklozenge$ , polyurethane sponge;  $\triangle$ , PTFE;  $\blacksquare$ , roughened PTFE walls.

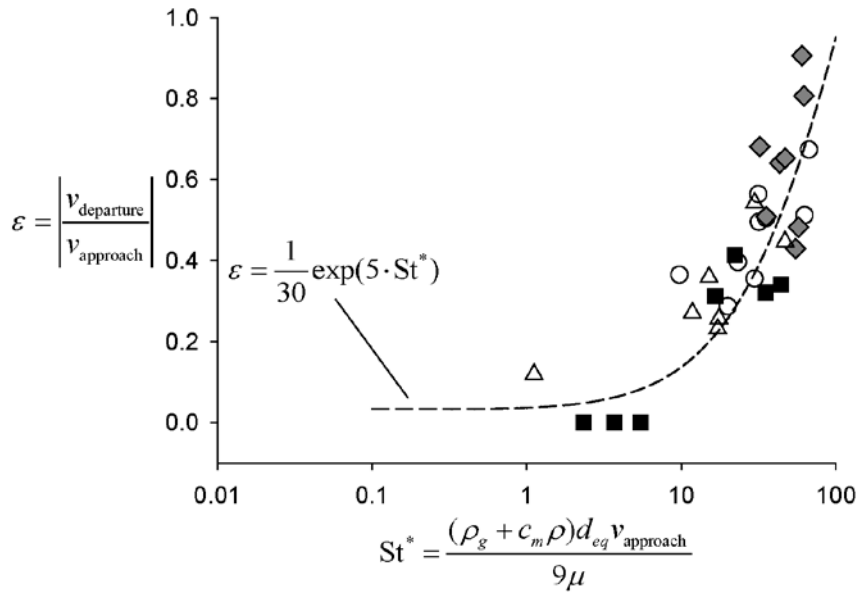


FIGURE 3.15 Variation of the coefficient of restitution ( $\varepsilon$ ) with the modified impact Stokes number ( $St^*$ ) for the rebounding and bouncing–sliding transition events;  $\circ$ , acrylic;  $\blacklozenge$ , polyurethane sponge;  $\triangle$ , PTFE;  $\blacksquare$ , roughened PTFE walls.

# Chapter 4

## Summary and Conclusion

In the present study, the rising bubble behaviour in the vicinity of the vertical wall has been investigated for a large deformable bubble. The current bubble has its own path instability which is two-dimensional zig-zag, without the wall. With the wall, more complex path instability appears from the interaction with the wall.

At small initial distances for no-slip and porous wall, the rebounding motion occurs with a regular bouncing amplitude and wavelength whereas the sliding motion occurs on the hydrophobic walls. The sliding motion is induced by the elongated contact duration between the bubble and the wall corresponding to the air pockets on the surface. As the initial distance increases, the rising bubble near the slip and hydrophobic wall becomes irregular motions and finally does not touch the wall. For porous walls, the rising bubble migrates away from the wall at smaller distance than other cases. For enhanced hydrophobic wall, the bubble initially bounces off the wall then the amplitude gradually decreases, finally the bubble slides on the wall.

In transports between the relevant energy components, the surface energy dominates the rising motion. The energy dissipation of sliding motion is larger than no-slip condition whereas the tangential slip condition has smallest energy loss. Also, the variation of the coefficient of restitution shows consistent trends showing the higher value for the porous condition and lower value for hydrophobic condition.

In present study, the general investigation of the rising bubble motion is suggested in terms of the motion and the energy analysis and it would helpful to understand the bubble–wall interactions. For more detailed understanding, the liquid velocity around the bubble should be measured. Also, because we simplify the bubble shape as the oblate ellipsoid, the more sophisticated investigation on this matter should be performed in future.

## Bibliography

- Batchelor, G. K. 1967 *An Introduction to Fluid Dynamics*. Cambridge: Cambridge University Press.
- Beavers, G. S. & Joseph, D. D. 1967 Boundary conditions at a naturally permeable wall. *J. Fluid Mech.* **30**, 197–207.
- Broder, D. & Sommerfeld, M. 2007 Planar shadow image velocimetry for the analysis of the hydrodynamics in bubbly flows. *Meas. Sci. Technol.* **18**, 2513–2528.
- Cassie, A. B. D. & Baxter, S. 1944 Wettability of porous surfaces. *Trans. Faraday Soc.* **40**, 546–551.
- Ellingsen, K. & Risso, F. 2001 On the rise of an ellipsoidal bubble in water: oscillatory paths and liquid-induced velocity. *J. Fluid Mech.* **440**, 235–268
- Ern, P., Risso, F., Fabre, D. & Magnaudet, J. 2012 Wake-induced oscillatory paths of bodies freely rising or falling in fluids. *Annu. Rev. Fluid Mech.* **44**, 97–121.
- Gangloff Jr., J. J., Hwang, W. R. & Advani, S. G. 2014 Characterization of bubble mobility in channel flow with fibrous porous media walls. *Int. J. Multiph. Flow.* **60**, 76–86.
- Gore, R. A. & Crowe, C. T. 1989 Effect of particle size on modulating turbulent intensity. *Int. J. Multiph. Flow* **15**, 279–285.
- Hahn, S., Je, J. & Choi, H. 2002 Direct numerical simulation of turbulent channel flow with permeable walls. *J. Fluid Mech.* **450**, 259–285.
- Hosokawa, S. & Tomiyama, A. 2013 Bubble-induced pseudo turbulence in laminar pipe flows. *Int. J. Heat Fluid Flow* **40**, 97–105.
- Krasowska, M. & Malysa, K. 2007 Kinetics of bubble collision and attachment to hydrophobic solids: I. effects of surface roughness. *Int. J. Miner. Process.* **81**, 205–216..
- Krishna, R., Urseanu, M. I., van Baten, J. M. & Ellenberger, J. 1999 Wall effects on the rise of single gas bubbles in liquids. *Int. Commun. Heat Mass Transf.* **26**, 781–790.
- Magnaudet, J. & Eames, I. 2000 The motion of high-reynolds-number bubbles in inhomogeneous flows. *Annu. Rev. Fluid Mech.* **32**, 659–708.
- Moctezuma, M. F., Lima-Ochoterena, R. & Zenit, R. 2005 Velocity fluctuations resulting from the interaction of a bubble with a vertical wall. *Phys. Fluids* **17**, 098106.

- Mougin, G. & Magnaudet, J. 2002 Path instability of a rising bubble. *Phys. Rev. Lett.* **88**, 014502.
- Mougin, G. & Magnaudet, J. 2006 Wake-induced forces and torques on a zigzagging/spiralling bubble. *J. Fluid Mech.* **567**, 185–194.
- Rensen, J., Luther, S. & Lohse, D. 2005 The effect of bubbles on developed turbulence. *J. Fluid Mech.* **538**, 153–187.
- Sadatoshi, T. 1956 Experimental investigation of the wake behind a sphere at low Reynolds numbers. *J. Phys. Soc. Japan.* **11**, 10.
- Sakamoto, H. & Haniu, H. 1990 A study on vortex shedding from spheres in a uniform flow. *J. Fluid Eng.* **112**, 386–392.
- Sheludko, A. 1967 Thin liquid films. *Adv. Colloid Interface Sci.* **1**, 391–464.
- Sugiyama, K. & Takemura, F. 2010 On the lateral migration of a slightly deformed bubble rising near a vertical plane wall. *J. Fluid Mech.* **662**, 209–231.
- Takemura, F. & Magnaudet, J. 2003 The transverse force on clean and contaminated bubbles rising near a vertical wall at moderate reynolds number. *J. Fluid Mech.* **495**, 235–253.
- Takemura, F., Takagi, S., Magnaudet, J. & Matsumoto, Y. 2002 Drag and lift forces on a bubble rising near a vertical wall in a viscous liquid. *J. Fluid Mech.* **461**, 277–300.
- Uno, S. & Kinter, R. C. 1956 Effect of wall proximity on the rate of rise of single air bubbles in a quiescent liquid. *AIChE J.* **2**, 420–425.
- de Vries, A. W. G. 2001 Path and wake of a rising bubble. PhD thesis, University of Twente, The Netherlands.
- Yang, B. & Prosperetti, A. 2007 Linear stability of the flow past a spheroidal bubble. *J. Fluid Mech.* **582**, 53–78.
- Zaruba, A., Lucasa, D., Prasser, H.-M. & Hohne, T. 2007 Bubble-wall interactions in a vertical gas.liquid flow: bouncing, sliding and bubble deformations. *Chem. Eng. Sci.* **62**, 1591–1605.
- Zawala, J., Krasowska, M., Dabros, T. & Malysa, K. 2007 Influence of bubble kinetic energy on its bouncing during collisions with various interfaces. *Can. J. Chem. Eng.* **85**, 669–678.
- Zenit, R. & Legendre, D. 2009 The coefficient of restitution for air bubbles colliding against solid walls in viscous liquids. *Phys. Fluids* **21**, 083306.
- Zenit, R. & Magnaudet, J. 2008 Path instability of rising spheroidal air bubbles: a shape-controlled process. *Phys. Fluids* **20**, 061702.

# 수직 벽 근처에서 상승하는 크기가 크고 변형가능한 기포의 움직임에 대한 실험적 연구

서울대학교 대학원

기계항공공학부

정현주

## 요약

본 연구에서는 수직 벽 근처에서 자유롭게 상승하는 기포의 거동을, 기포-벽 간 초기 거리와 벽의 재질 등 벽의 조건들을 변화시키며 측정하고 분석하였다. 기포의 레이놀즈 수와 웨버 수는 기포의 반지름을 기준으로 각각 1100, 4.4 이며 선행연구에 비해 큰 값을 가진다. 연구에 쓰인 기포는 기본적으로 형태가 일정치 않으며 2차원의 지그재그 궤적으로 진동하며 상승한다. 기포-벽 간 초기 거리와 벽 표면 재질이 벽의 영향을 보기 위한 변수로 사용되었다. 기포가 벽 근처를 상승하면서, 기포는 튀어오름, 미끄러짐 등 다양한 움직임을 보여주면서도 2차원성을 유지함을 확인하였다. 상승하는 기포의 움직임에서, 특히 벽 표면 재질이 기포의 거동에 큰 영향을 미친다. 따라서 본 연구에서는 사인 함수를 사용하여 튀어오르는 기포에 대한 연구를 수행하고 각 기포의 움직임에 대한 에너지 성분들을 분석하였다. 에너지 소산은 기포-벽간 초기 거리와 벽 재질에 따라서 다른 경향을 보여주게 되는데, hydrophobic한 조건의 경우, 기포가 벽을 따라 미끄러질 때, no-slip 조건에 비하여 큰 에너지 소산을 발생시키는 것을 관찰하였다. 기포-벽간 거리가 상승하게 되면 기포는 벽과 충돌하지 않게 되며 이 때는 오히려 에너지 소산이 감소하게 된다. 반면 porous 조건의 경우, 에너지 소산은 실험 조건 중

가장 적은 값을 가지게 된다. 또한 더 심도있는 분석을 위하여 반환계수가 계산되었고 이는 에너지 분석과 일치하는 경향성이 나타난다.

**주요어:** 기포-벽 상호작용, 벽의 효과, 궤적 불안정성, 벽 표면 재질, 튀어오름, 미끄러짐

**학번:** 2013-20717